Available online at www.sciencedirect.com
SCIENCE DIRECT®
International Journal of Heat and Fluid Flow 26 (2005) 681–694
International Journal of HEAT AND FLUID FLOW
www.elsevier.com/locate/ijhff

Large eddy simulation of turbulent flow and heat transfer in a channel with one wavy wall

Hang Seok Choi [a], Kenjiro Suzuki [b,*]

[a] Department of Mechanical Engineering, Kyoto University, Kyoto 606-8501, Japan
[b] Department of Machinery and Control Systems, Shibaura Institute of Technology, 307 Fukasaku, Saitama 337-8570, Japan

Received 13 May 2004; accepted 8 March 2005
Available online 24 May 2005

Abstract

Large eddy simulation (LES) has been applied to turbulent thermal fields in a channel having one wavy wall for Prandtl number = 0.7. Wall wave amplitude is changed in three steps. Increasing the wall wave amplitude, a flow separation bubble comes to appear and a separated turbulent shear layer develops above the separation bubble. Additionally, in the up-slope region of the bottom wavy wall, near-wall streamwise vortices are generated with larger population. These two turbulence features, i.e., the separated shear layer and the near-wall streamwise vortex, play an important role for the heat and momentum transfer near the wavy wall. So, the characteristics of the separated shear layer and the near-wall streamwise vortices are discussed in relation to the turbulent heat transfer. For this purpose, vortical flow structures aligned toward the streamwise direction and turbulent thermal fields around the vortices were captured and the statistical quantities relating to the turbulent thermal fields were scrutinized. Especially, attention is paid to the effect of the near-wall streamwise vortices on the turbulent heat transfer and the conditionally averaged patterns of turbulent thermal fields around the streamwise vortices were established. The results obtained indicate that the near-wall streamwise vortices produce the strong events of Q_{T4} and Q_{T6}. Here, Q_{T4} and Q_{T6} are cold sweep-like motion and hot ejection-like motion, respectively. Especially, Q_{T4} event makes the gradient of fluid temperature near the wall steeper in the up-slope region and consequently enhances the heat transfer at the bottom wavy wall. Furthermore, with increasing the wall wave amplitude, the near-wall streamwise vortices were strengthened and as a result the wavy wall heat transfer is more noticeably enhanced. In practical view point, if pumping power is kept the same, better heat transfer performance can be achieved with increasing wall wave amplitude.

Keywords: Wavy wall; Turbulent heat transfer; Large eddy simulation; Near-wall streamwise vortex

1. Introduction

In various heat transfer devices, enhancement of wall heat transfer is a key requirement to make the devices compact or effective. One of the typical techniques for heat transfer enhancement in such devices is to introduce wall undulation for heat transfer surfaces. Present study is an extension of the previous works (Choi et al., 2004; Park et al., 2004) on the turbulent flows and related heat transfer in a channel having one wavy wall for $Pr = 0.7$. This study aims at analyzing the characteristics of the flows and related heat transfer applying the large eddy simulation (LES). The present article particularly discusses how the near-wall streamwise vortices appearing densely in the up-slope part of the wall and repeating birth and disappearance after a certain length of life affect the wall heat transfer. Discussions on statistical characteristics of the turbulent flow are found in the reference (Choi, 2004).

Flows along wavy walls are also of importance both from scientific and practical view points in relation to environmental and engineering problems. They display

* Corresponding author. Tel.: +81 48 687 5115; fax: +81 48 687 5197.
E-mail address: ksuzuki@sic.shibaura-it.ac.jp (K. Suzuki).

0142-727X/$ - see front matter © 2005 Elsevier Inc. All rights reserved.
doi:10.1016/j.ijheatfluidflow.2005.03.001

Nomenclature

a	wave amplitude
C_f	time mean local skin friction coefficient
C_p	specific heat at constant pressure
D_h	hydraulic diameter
d^*_{VN}	spanwise distance between a vortex centerline and Nu_{D_h} peak position line
F_1	time and spatial mean pressure gradient driving the flow in a channel
f	friction factor, $f = 4(\partial P/\partial x)H/(\rho U_b^2)$
H	channel height
$\hat{h}_j$	subgrid-scale heat flux
k_f	fluid conductivity
L	channel length
l^*_{vortex}	the streamwise length of a vortex centerline
$l^*_{Nu_{D_h}}$	the streamwise length of a Nu_{D_h} peak position line
Nu_{D_h}	Nusselt number, $Nu_{D_h} = hD_h/k_f = q''_w D_h/k_f(\Theta_w - \Theta_b)$
Nu	time mean local Nusselt number
$\overline{Nu}$	time and space mean Nusselt number
Nu_{trough}	time and space mean Nusselt number only for trough region of the bottom wavy surface
P	mean pressure
P_{pw}	pumping power, $P_{pw} = f^{1/3}Re_b$
Pr	Prandtl number
$\hat{p}$	filtered pressure
Q_{T4}	the fourth octant of Reynolds transverse heat flux in u–v–θ space
Q_{T6}	the sixth octant of Reynolds transverse heat flux in u–v–θ space
Q_{V4}	the fourth octant of Reynolds shear stress in u–v–θ space
Q_{V6}	the sixth octant of Reynolds shear stress in u–v–θ space
q''_w	wall heat flux
Re_b	Reynolds number, $Re_b = (U_b \cdot H)/\nu$
Re_Γ	vortex circulation Reynolds number, $Re_\Gamma = \Gamma/\nu$
t	time
U_b	bulk mean velocity
U_i	mean velocity
u_i	velocity fluctuation
$\tilde{u}_i$	instantaneous velocity
u'_i	rms velocity fluctuation
$\hat{u}_i$	filtered velocity
u_τ	friction velocity at the bottom wavy wall
$\overline{u_i u_j}$	Reynolds stress
W	channel width
y_w	transverse location of bottom wavy wall surface
z_c	spanwise location of a sampled centerline of a vortex

Greek symbols

α	thermal diffusivity
Γ	circulation
λ	wavelength
Λ_2	the second largest eigenvalue of $S_{ik}S_{kj} + \Omega_{ik}\Omega_{kj}$
ν	kinematic molecular viscosity
ρ	fluid density
Θ	mean temperature
Θ_b	bulk mean temperature
Θ_w	wall temperature
θ	temperature fluctuation
θ'	rms temperature fluctuation
$\hat{\theta}$	filtered temperature
$\tilde{\theta}$	instantaneous temperature
θ_{VN}	angle between a vortex centerline and Nu_{D_h} peak position line
θ_τ	friction temperature, $\theta_\tau = q''_w/(\rho C_p u_\tau)$
$\hat{\tau}_{ij}$	subgrid-scale stress tensor
$\langle \tilde{\omega}_s(\partial \tilde{u}_s/\partial s)\rangle_c$	vortex stretching term

Symbols

$\langle\ \rangle_c$	conditional averaging process along a vortex centerline or Nu_{D_h} peak position line
$\langle\ \rangle_{cs}$	conditional averaging process for (y,z) cross-sectional plane at a streamwise position

peculiar characteristics that are not observed in the flows over a flat plate surface. In the case of wavy wall channel flows, the periodic changes of pressure gradient and of streamline curvature generate turbulence structure different from the counterpart of flat plate channel flows. Furthermore, if the wall wave amplitude and Reynolds number are increased, a flow separation bubble appears near the trough region of the wavy wall and a separated shear layer formed slightly above the separation bubble raises the turbulence intensity. Another important aspect of the flows over a wavy wall is near-wall vortical fluid motions appearing near the up-slope region which are aligned with the streamwise direction (De Angelis et al., 1997; Choi et al., 2004; Henn and Sykes, 1999). These flow characteristics should influence the transport pattern of the passive scalar as well as of the momentum in such flows.

The role of an organized vortex on heat transfer has been widely studied by many researchers (Eibeck and Eaton, 1987; Inaoka and Suzuki, 1995; Suzuki, 1996; Suzuki et al., 1998; Suzuki and Nakabe, 2002; Vold, 1999; Wroblewski and Eibeck, 1991). Especially, for

the longitudinal vortex embedded in a turbulent boundary layer, thinning of the thermal boundary layer occurs at the down-wash side positions of the vortex and enhances the wall heat transfer (Eibeck and Eaton, 1987; Inaoka and Suzuki, 1995; Wroblewski and Eibeck, 1991). Kasagi and Ohtsubo (1995) carried out the direct numerical simulation for the turbulent thermal field in a flat plate channel flow, and they showed the deep relationship between streamwise vortices and near-wall turbulent heat transfer. For wavy wall channel flows, some numerical studies (Matsubara et al., 2002; Park et al., 2004) have been carried out in order to clarify the effect of the wall undulation on the characteristics of the turbulent heat transfer, but close attention has not yet been given to the role of the near-wall streamwise vortices on the heat transfer. As is demonstrated in the reference (Choi et al., 2004), the near-wall streamwise vortices appearing in the up-slope region should affect the heat transfer in the wavy wall channel flows. So, the present LES study aims at giving insight to the effect of the near-wall streamwise vortices on the turbulent heat transfer in a wavy wall channel flow.

2. Mathematical formulation

The filtered forms of the continuity equation and the momentum equations for incompressible fluid are expressed as follows:

$$\frac{\partial \hat{u}_i}{\partial x_i} = 0, \tag{1}$$

$$\frac{\partial \hat{u}_i}{\partial t} + \hat{u}_j \frac{\partial \hat{u}_i}{\partial x_j} = \nu \frac{\partial^2 \hat{u}_i}{\partial x_j \partial x_j} - \frac{\partial \hat{\tau}_{ij}}{\partial x_j} - \frac{1}{\rho}\frac{\partial \hat{p}}{\partial x_i} + F_1 \delta_{1i}, \tag{2}$$

where $\hat{u}_i$, $\hat{p}$ and $\hat{\tau}_{ij}$ are filtered velocity, filtered pressure and subgrid-scale stress tensor, respectively. The subgrid-scale stress tensor is defined as $\hat{\tau}_{ij} \equiv \widehat{u_i u_j} - \hat{u}_i \hat{u}_j$ and F_1 is the time and spatial mean pressure gradient driving the flow in the channel to be studied. The filtered form of the energy equation used in the present study is expressed as follows:

$$\frac{\partial \hat{\theta}}{\partial t} + \hat{u}_j \frac{\partial \hat{\theta}}{\partial x_j} = \frac{\partial}{\partial x_j}\left[\frac{\nu}{Pr}\frac{\partial \hat{\theta}}{\partial x_j} - \hat{h}_j\right], \tag{3}$$

where $\hat{\theta}$ is filtered temperature and $\hat{h}_j$ is the subgrid-scale heat flux defined as $\hat{h}_j \equiv \widehat{u_j \theta} - \hat{u}_j \hat{\theta}$. The Prandtl number is set as $Pr = 0.7$. In Eqs. (2) and (3), $\hat{\tau}_{ij}$ and $\hat{h}_j$ must be modelled.

The subgrid-scale eddy viscosity model firstly introduced by Smagorinsky (1963) has been popularly used for $\hat{\tau}_{ij}$ and $\hat{h}_j$ but, one major drawback of this model is its inability to correctly represent various turbulent flow fields with a single model constant. To eliminate this deficiency, the dynamic subgrid-scale model was suggested by Germano et al. (1991). This dynamic subgrid-scale model was modified by Lilly (1992) by making use of the least square technique to minimize the difference between the closure assumption and the resolved stresses. The present LES study adopts the dynamic subgrid-scale model of Lilly (1992) for both $\hat{\tau}_{ij}$ and $\hat{h}_j$.

3. Numerical methods

3.1. Numerical procedure

To numerically solve the finite-difference equivalents of Eqs. (1) and (2), semi-implicit fractional step method is used. So, the time integration of the discretized governing equations are carried out based on the hybrid scheme using an Adams–Bashforth method for explicitly treated terms and a Crank–Nicolson method for implicitly treated terms. The explicitly treated terms are the convection terms, the diffusion terms with cross-derivatives and the source terms, and the implicitly treated ones are the diffusion terms without cross-derivatives. As for the spatial discretization of Eq. (2), the sixth-order COMPACT scheme (Lele, 1992) for the convective terms, and the fourth-order central differencing for the diffusion terms and other remaining terms are applied. In the present study, non-staggered grid system is adopted, so the momentum interpolation technique (Park, 1999) is employed to avoid the pressure–velocity decoupling. For the filtered energy equation, the respective terms are treated in the same way as the corresponding terms of the momentum equations except for the convection terms. For the convection terms of Eq. (3), HLPA scheme (Zhu, 1992) is used. Details of this hybrid scheme can be found in You et al. (2000).

3.2. Computational condition

Fig. 1 shows the computational domain together with the coordinate system and the geometrical parameters adopted in the present study. L, W, and H represent the streamwise, spanwise and transverse or wall-normal length of the computational domain. The bottom wall of the channel has the sinusoidal undulation having amplitude a and wavelength λ, and its mean position is located at $y = 0$. The bottom wall position is therefore given by $y_w = a\cos(2\pi x/\lambda)$ and the top wall is flat and located at $y = H$. Computation has been made for the three cases of different amplitude to wavelength ratio of wall undulation $a/\lambda = 0.01$, 0.05, and 0.1 keeping the flow Reynolds number constant, i.e., $Re_b = (U_b \cdot H)/\nu = 6760$. The values of other geometrical parameters and information about the grid allocation are given in Table 1. Here wall unit is calculated with the friction velocity based on the mean wall shear stress

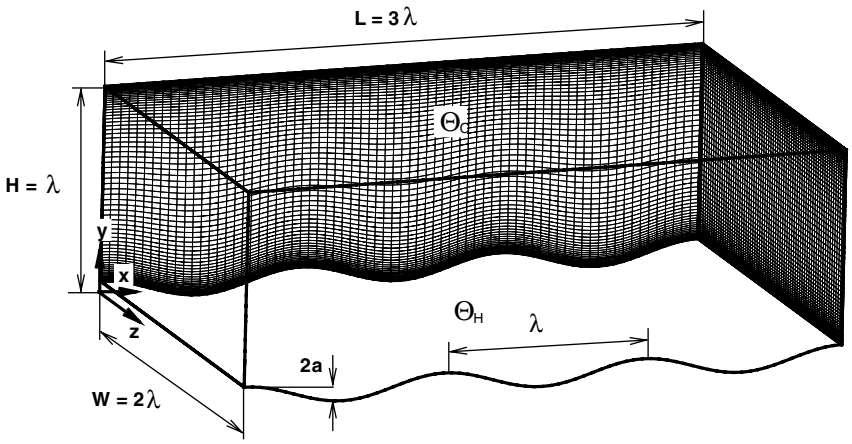

Fig. 1. Computational domain.

Table 1
Calculation conditions

Case	Re_b	L/λ (L/H)	W/λ (W/H)	Grid no.	a/λ	Δy^+_{min}	Δy^+_{max}	Δx^+	Δz^+
Flat 1	4580	π	π/H	$34\times66\times34$	0.0	1.5	10.6	37.7	18.8
Flat 2	6760	π	π/H	$34\times66\times34$	0.0	1.5	10.6	37.7	18.8
W001	6760	3	2	$74\times66\times66$	0.01	1.6	11.4	16.9	12.7
W005	6760	3	2	$74\times66\times66$	0.05	1.4	10.4	14.9	11.2
W01	6760	3	2	$74\times66\times66$	0.1	0.9	7.3	9.9	7.5

Flat 1: isoflux wall boundary condition corresponding to Kasagi et al. (1992); Flat 2: isothermal wall boundary condition.

averaged over the whole wavy wall surface. The results of Choi et al. (2004) are used as the initial condition for the fully developed turbulent flow fields of the wavy wall channel to calculate the thermal fields. For the boundary conditions, a no-slip condition is used at both the top and bottom walls and a spatially periodic boundary condition is applied to the spanwise and streamwise directions. For the thermal wall boundary conditions, a constant temperature condition is applied. So, the flat wall is maintained at a constant temperature Θ_C, while the wavy wall is heated at an another constant temperature Θ_H.

3.3. Validation of the present LES

Validation of the present LES has been performed for the turbulent flow fields in a wavy wall channel in the previous work (Choi et al., 2004). For the purpose to further validate the present LES for the calculation of turbulent thermal fields, turbulent heat transfer in a flat plate channel flow is treated. Fig. 2 shows the comparison of the predicted Θ/θ_τ, θ'/θ_τ, $\overline{u\theta}/(u_\tau\theta_\tau)$, and $-\overline{v\theta}/(u_\tau\theta_\tau)$ with the DNS results of Kasagi et al. (1992). Here, Θ, θ', θ_τ, $\overline{u\theta}$ and $\overline{v\theta}$ are the mean temperature, root mean square (hereinafter abbreviated as rms) value of temperature fluctuation, friction temperature, streamwise turbulent heat flux and transverse turbulent heat flux, respectively. In this computation, the Reynolds number is $Re_b = (U_b \cdot H)/\nu = 4580$ and the grid number is $34\times66\times34$. The values of other geometrical parameters and information about the grid allocation for this computation are given in Table 1. All the plotted results show that the present LES results agree well with the DNS data of Kasagi et al. (1992). Combining this comparison with another comparison made in the previous study, the present LES is judged to give reasonable results for the turbulent flows and related heat transfer in a wavy wall channel.

3.4. Processing of numerical results

3.4.1. Identification of vortex core and conditionally sampled related quantities

In order to capture the streamwise vortices appearing near the wavy wall, the method of Jeong and Hussain (1995) and Jeong et al. (1997) is applied in the present study. At every grid point and at every time step, calculation was made for finding a quantity Λ_2, the second largest one among the three eigenvalues of $-(1/\rho)(\partial^2\tilde{p}/\partial x_i\partial x_j)$ or specifically of its equivalent $S_{ik}S_{kj} + \Omega_{ik}\Omega_{kj}$, where Ω_{ik} and Ω_{kj} are the vorticity tensor and S_{ik} and S_{kj} the strain rate tensor. At each instant, attention was paid to the value of Λ_2 calculated at the grid points of the near-wall region, $0 \leqslant (y - y_w)/H \leqslant 0.2$ in the following manner. Among the positions where Λ_2 takes negative value in that region, the ones where Λ_2

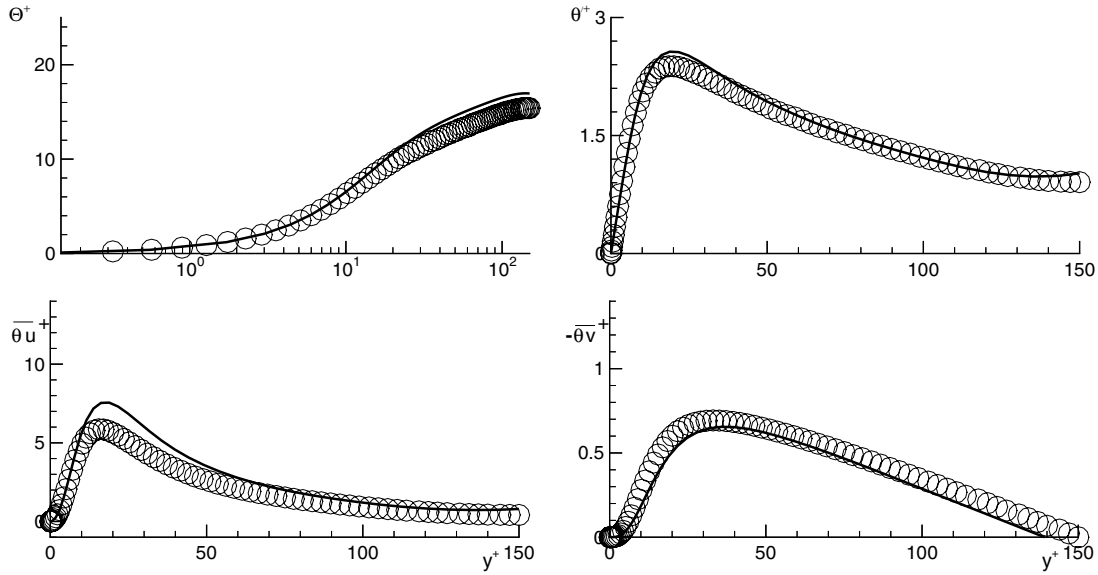

Fig. 2. Comparison of the predicted Θ/θ_τ, θ'/θ_τ, $\overline{u\theta}/(u_\tau\theta_\tau)$ and $-\overline{v\theta}/(u_\tau\theta_\tau)$ with the DNS results of Kasagi et al. (1992) (DNS : ○, LES : —); + indicates the non-dimensional value normalized by wall units.

takes local minimum value were scrutinized. All the detected positions of the local minimum of Λ_2 values were identified as the central positions of locally existing vortices. Finally, centerlines of the vortices were constructed as the lines connecting one center position in one cross-section to another in neighboring cross-section if they are aligned with the streamwise direction within the maximum tilting and inclined angles of 40°. This method assumes firstly that a local pressure minimum corresponds to a vortex center, secondly that negative Λ_2 represents the concavity of the pressure distribution around the vortex major axis and lastly that the local pressure minimum position is approximately represented by the local minimum position of Λ_2. In the statistical study of the numerical results to follow, attention has been paid to the vortices having the centerline length $l^*_{\text{vortex}} = l_{\text{vortex}}/\lambda \geqslant 1/8$. Fig. 3 shows a schematic of a vortex lying near the wall and its projection onto the wavy wall.

As will be discussed later, instantaneous local Nusselt number, Nu_{D_h}, is distributed non-uniformly on the wavy wall. In fact, a number of spindle-shape high Nusselt number regions appear and keep their identity for a certain period of time before their disappearance. Their locations are represented by a line connecting the Nu_{D_h} peak positions inside the high Nu_{D_h} region as also illustrated in Fig. 3. Close attention is paid to the lines having the streamwise length larger than a threshold value, i.e., $l^*_{Nu_{D_h}} = l_{Nu_{D_h}}/\lambda \geqslant 1/8$ again and aligned with the centerlines of the detected streamwise vortices, or more specifically, with the positions of the vortex centerlines projected onto the wavy wall surface.

Typical patterns of velocity and thermal fields around the vortex have been established in cross-sections adjacent to the bottom wavy wall having the size of height $0.17H$ from the wall and width $0.34H$ by making use of the following conditional average.

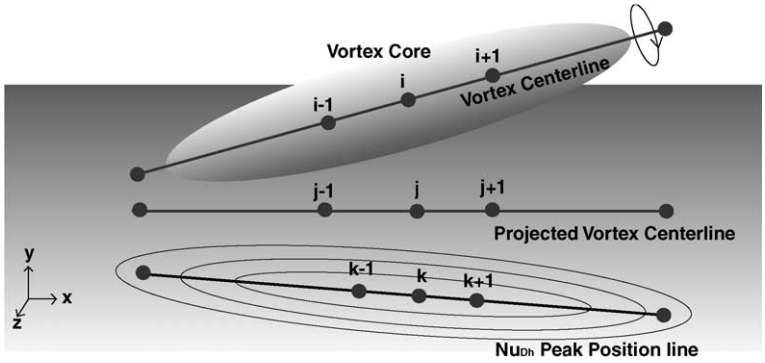

Fig. 3. Schematic diagram for a vortex core, vortex centerline and Nu_{D_h} peak position line.

$$\langle q(\mathbf{x}^*,t)\rangle_{cs} = \langle q(x^*,y^*,z^*,t)\rangle_{cs} = \frac{1}{N}\sum_{i=1}^{N} q(x/\lambda,(y-y_w)/H,(z-z_c)/\lambda,t), \quad (4)$$

where $\langle\ \rangle_{cs}$ indicates the conditional averaging in a cross-section, q represents a flow or thermal quantity to be studied, z_c is the spanwise position of a sampled centerline of a vortex and N is the total number of the sampled vortices. The present conditional average will be used in the discussion on how the generation of near-wall streamwise vortices is related to the characteristics of wall heat transfer especially in the up-slope region. So, in the following, discussions will be developed for the statistical cross-sectional patterns of velocity and temperature fields obtained at a position $x/\lambda = 0.94$ located in the up-slope part of the wavy wall.

In addition to the quantities mentioned above, several different types of probability density functions were constructed. They are as follows:

- streamwise length of a vortex centerline, l^*_{vortex};
- streamwise length of a line connecting the Nu_{D_h} peak positions, $l^*_{Nu_{D_h}}$;
- spanwise distance between a vortex centerline and the nearest Nu_{D_h} peak position line, d^*_{VN};
- tilting angle of a Nu_{D_h} peak position line from the closest vortex centerline, θ_{VN};
- spatial mean of the peak value of Nu_{D_h} averaged along the Nu_{D_h} peak position line, $\langle Nu_{D_h}\rangle_c$;
- spatial mean vortex circulation Reynolds number averaged along the vortex centerline, $\langle Re_\Gamma\rangle_c$;
- spatial mean vortex stretching term averaged along the vortex centerline, $\langle\tilde{\omega}_s(\partial\tilde{u}_s/\partial s)\rangle_c$.

Here, the superscript "*" indicates the non-dimensional value normalized with λ, and $\langle\ \rangle_c$ represents the value which is averaged along a vortex centerline or Nu_{D_h} peak position line. Hereafter, probability density function will be abbreviated as pdf for simplicity.

In computing the value of $\langle Re_\Gamma\rangle_c$, circulation Γ was first calculated at each streamwise position for each vortex as the integral of the vorticity over the cross-sectional (y,z) plane within the vortex core. Here, as discussed above the vortex core was defined as the region where Λ_2 takes negative value smaller than a certain value. Then, the local value of the vortex circulation Reynolds number was obtained by dividing the calculated circulation by kinematic viscosity as $Re_\Gamma = \Gamma/\nu$ according to Westphal et al. (1987). For the space mean vortex stretching term, $\langle\tilde{\omega}_s(\partial\tilde{u}_s/\partial s)\rangle_c$, the vortex stretching term in the vorticity equation can be represented along the curve of the vortex centerline as follows (Kida and Yanase, 2000):

$$(\tilde{\boldsymbol{\omega}}\cdot\nabla)\tilde{\mathbf{u}} = \tilde{\omega}_s[(\partial\tilde{u}_s/\partial s - \chi\tilde{u}_n)\mathbf{s} + (\chi\tilde{u}_s + \partial\tilde{u}_n/\partial s - \tau\tilde{u}_b)\mathbf{n} + (\tau\tilde{u}_n + \partial\tilde{u}_b/\partial s)\mathbf{b}]. \quad (5)$$

Here s, n and b represent the each coordinate direction of curvilinear orthogonal coordinate system. In particular, s is the direction along the vortex centerline. $\tilde{u}_s$, $\tilde{u}_n$ and $\tilde{u}_b$ are the velocity components respectively along s, n and b directions, and χ and τ are the curvature and torsion obtained from the Frenet–Seret formula, respectively. In Eq. (5), the vortex stretching term, $\tilde{\omega}_s(\partial\tilde{u}_s/\partial s)$, is only calculated at each vortex center point along a vortex centerline. For these pdfs, the mean of each variable q is obtained as follows:

$$\text{Mean value of } q = \int_{-\infty}^{\infty} q\cdot\mathrm{pdf}(q)\,\mathrm{d}q. \quad (6)$$

3.4.2. Octant analysis

Octant analysis (Suzuki et al., 1988) has been applied by sampling the instantaneous values of streamwise and transverse fluctuating velocity components and temperature fluctuation in order to see which of the elementary patterns of the coherent turbulent fluid motion is a major contributor to the momentum or heat transfer, especially around near-wall streamwise vortices appearing in the up-slope region. In the discussions to follow, among eight octants described in Table 2 four instantaneous local quantities Q_{V4}, Q_{V6}, Q_{T4} and Q_{T6} appear. They are defined as follows:

$$Q_{Vi} = \langle uv\rangle_i = \frac{1}{N}\sum_{j=1}^{N} I_i(j)u_jv_j, \quad (7)$$

where $\langle\ \rangle_i$ specifies the contribution to the Reynolds shear stress, $\overline{uv}$, from the events to be assigned to the ith octant of u–v–θ space. u_j and v_j are the jth sample of u and v fluctuating velocity components. N is the total number of samples. $I_i(j) = 1$ when the signs of u_j and v_j

Table 2
Octant analysis (Suzuki et al., 1988)

First octant	Cold outward interaction	$u>0$, $v>0$, $\theta<0$	Q_{V1} or Q_{T1}
Second octant	Cold ejection-like motion	$u<0$, $v>0$, $\theta<0$	Q_{V2} or Q_{T2}
Third octant	Cold wall-ward interaction	$u<0$, $v<0$, $\theta<0$	Q_{V3} or Q_{T3}
Fourth octant	Cold sweep-like motion	$u>0$, $v<0$, $\theta<0$	Q_{V4} or Q_{T4}
Fifth octant	Hot outward interaction	$u>0$, $v>0$, $\theta>0$	Q_{V5} or Q_{T5}
Sixth octant	Hot ejection-like motion	$u<0$, $v>0$, $\theta>0$	Q_{V6} or Q_{T6}
Seventh octant	Hot wall-ward interaction	$u<0$, $v<0$, $\theta>0$	Q_{V7} or Q_{T7}
Eighth octant	Hot sweep-like motion	$u>0$, $v<0$, $\theta>0$	Q_{V8} or Q_{T8}

match the counterpart of ith octant of u–v–θ space and otherwise $I_i(j) = 0$. Q_{V4} represents the cold sweep-like motion and Q_{V6} the hot ejection-like motion.

In a similar manner to the above definition of Q_{Vi}, Q_{T4} and Q_{T6} are defined as follows:

$$Q_{Ti} = \langle v\theta \rangle_i = \frac{1}{N} \sum_{j=1}^{N} I_i(j) v_j \theta_j, \tag{8}$$

where the suffix i specifies the octant of u–v–θ space. Q_{T4} represents the cold sweep-like motion and Q_{T6} the hot ejection-like motion.

4. Results and discussion

4.1. Overall pressure loss characteristics and heat transfer performance

Here first the overall flow and heat transfer performance of the flow inside the channel having one wavy wall will be discussed, namely the time mean local skin friction coefficient C_f, the time mean local wall Nusselt number Nu and the non-dimensional pumping power $P_{pw} = f^{1/3} Re_b$ to maintain the flow through the channel (Matsubara et al., 2002). Fig. 4 shows the streamwise distributions of C_f and Nu on the bottom wavy wall. As can be seen from the figure, both of C_f and Nu have the maximum value in the up-slope part of the wavy wall. Wall undulation is found to effectively enhance the wall heat transfer. With the increase of the wave amplitude from $a/\lambda = 0.01$ to $a/\lambda = 0.1$, C_f peak value becomes about three times larger and Nu peak value about four times larger. In Fig. 5(a) and (b) is plotted the time and space mean Nusselt number $\overline{Nu}$ obtained by averaging over the whole wavy bottom surface, respectively, against the pumping power P_{pw} and the flow Reynolds number Re_b. In those figures, the values for flat plate channel flow are also presented. In addition to the solid line given by Mills (1992) for the flat plate channel case, the present results of the Flat 2 case obtained by applying LES are also included. As is found in Fig. 5, increasing the wall wave amplitude from the case W001 to the case W01, $\overline{Nu}$ increases at a larger rate

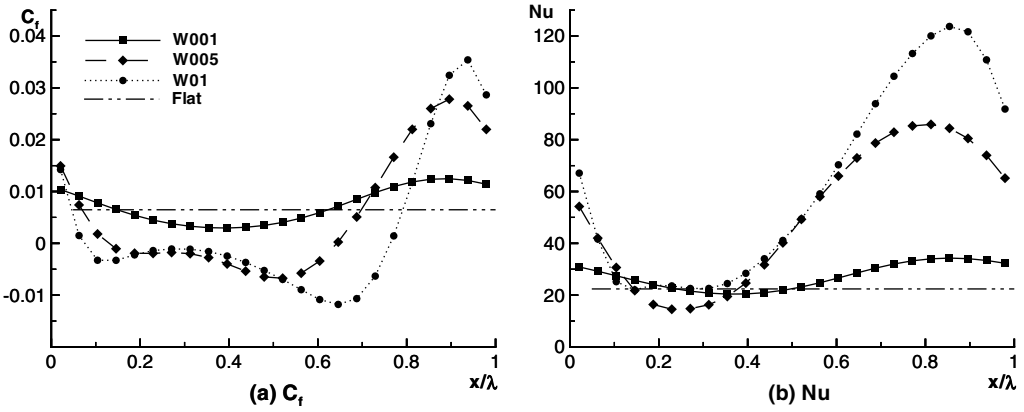

Fig. 4. Distributions of time mean local skin friction coefficient, C_f, and time mean local wall Nusselt number, Nu, along the streamwise direction with varying wall wave amplitude.

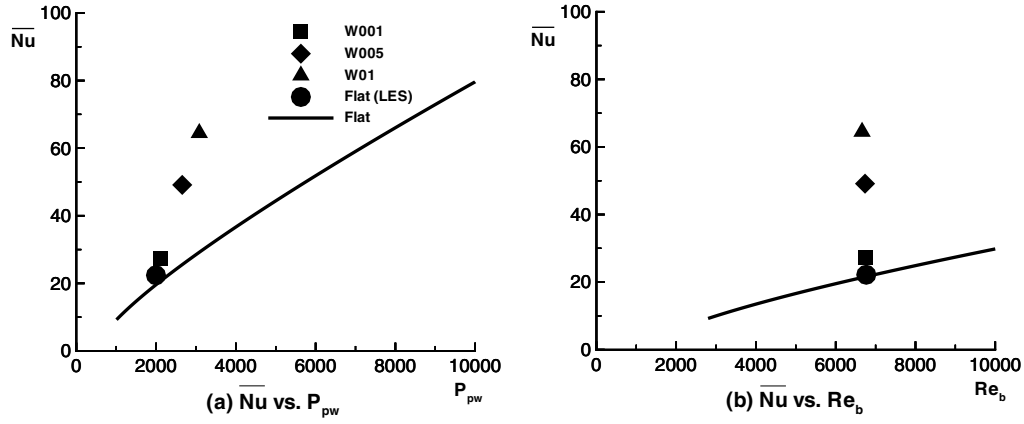

Fig. 5. Overall characteristics of heat transfer and related performance with varying wall wave amplitude.

than P_{pw} does. This indicates that if the pumping power is kept the same, better heat transfer performance can be achieved with a channel having wavy wall and heat transfer performance becomes better if wave amplitude is increased more.

4.2. Effect of near-wall streamwise vortices on heat transfer

As has been discussed by Choi et al. (2004), ejection type and sweep type motions appear around the near-wall streamwise vortices. They are found to, respectively, produce the outward fluid motion carrying the low speed fluid lumps toward the high speed flow region and in opposite way the wall-ward fluid motion feeding the high speed fluid lumps toward the low speed flow region. These motions have a significant effect on the momentum transfer around the vortices. These vortices are generated with larger population within the up-slope region. These fluid motions should also assist the heat transfer around the streamwise vortices and thus are expected to affect the heat transfer in the region near the wavy wall surface, especially, in the up-slope part of the wavy wall. This is now discussed taking into account the results obtained in this Large Eddy Simulation. Unless otherwise mentioned, all the quantities in the following figures represent the non-dimensional values normalized with U_b, the bulk mean velocity, and $\Delta\Theta = \Theta_H - \Theta_C$, the temperature difference between the bottom wavy wall and top flat wall.

Fig. 6(a) shows again the distributions of the time mean local Nusselt number Nu and the time mean friction coefficient C_f on the wavy bottom wall surface for W01 case. Nu shows much larger value in the up-slope part of the wavy wall and C_f takes negative value within a flow separation bubble lying from $x/\lambda = 1.08$ to 1.76 as already discussed in Choi et al. (2004). Fig. 6(b)–(d) shows the instantaneous results obtained for the same case. Fig. 6(b) particularly illustrates the distribution of the instantaneous Nusselt number Nu_{D_h} on the bottom surface and a number of high Nu_{D_h} spindle-shaped spots are observed in the up-slope part of the bottom wall. This is related to the higher value of Nu in the up-slope part of the bottom wavy wall as has been observed in Fig. 4(b). In Fig. 6(c) and (d) the instantaneous near-wall cross-sectional patterns of the velocity and temperature fields are presented, obtained in the region of $0.5 \leqslant z/\lambda \leqslant 1.0$ at the streamwise position $x/\lambda = 1.8$. Fig. 6(c) shows the secondary flow velocity map and Fig. 6(d) shows the fluid temperature contours both together with the contour of Λ_2. At the bottom of Fig. 6(d) is also included the spanwise distribution of instantaneous Nusselt number

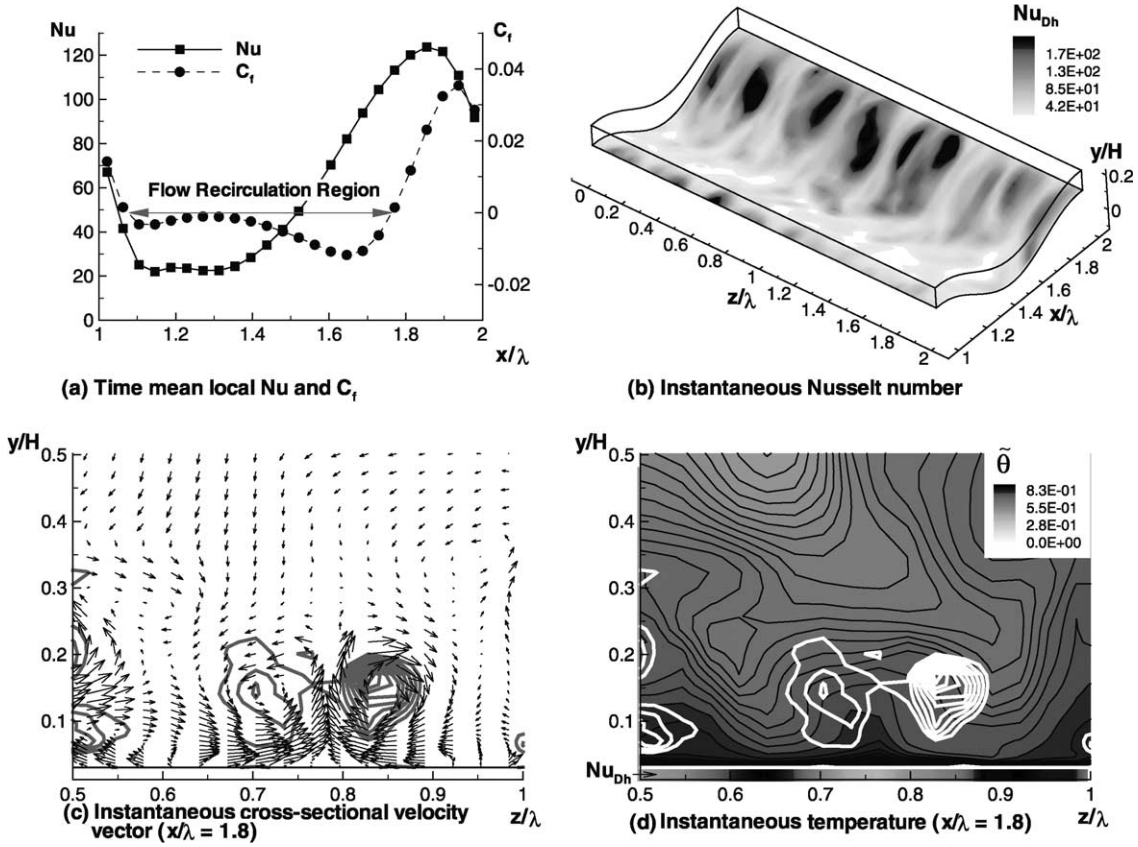

Fig. 6. Time mean local quantities and instantaneous turbulent flow and thermal fields in the case of W01.

on the wavy wall surface at $x/\lambda = 1.8$. As is seen in the middle bottom region of Fig. 6(c), a mushroom like secondary flow pattern is generated near the wall in between the counter-rotating vortices which are well captured by Jeong's Λ_2 method. Around the vortices, down-wash flows exist on both sides of the vortices. At positions almost beneath the down-wash flows, temperature boundary layer is thin and Nu_{D_h} takes high value there. In between the vortices, inward flows meet very near the wall and then up-wash flow is generated. Temperature boundary layer becomes thick and Nu_{D_h} remains low there. However, time and space mean Nusselt number $\overline{Nu}$ increases if the wall undulation is introduced since significant heat transfer enhancement is obtained beneath the down-wash flow region. This will be revisited and discussed more in detail later.

More detailed discussions are now developed as for the role of the streamwise vortices, appearing in the up-slope part of the wavy wall, on the heat transfer enhancement to be produced by the wall waviness. Fig. 7 shows four probability density functions, the streamwise length of a vortex centerline l^*_{vortex} in (a), the streamwise length of a line connecting the Nu_{D_h} peak positions $l^*_{Nu_{D_h}}$ in (b), the spanwise distance between a vortex centerline and the nearest Nu_{D_h} peak position line d^*_{VN} in (c) and the tilting angle of a Nu_{D_h} peak position line raised from the closest vortex centerline θ_{VN} in (d) for the case W005. In this figure, results both for clockwise and counter-clockwise vortices are plotted. CCW represents the counter-clockwise one and CW the clockwise one. It is clear that there is no statistical difference between the clockwise one and counter-clockwise one. Detected streamwise vortices and spindle-shaped high Nu_{D_h} spots have almost the same length and lie almost in parallel closely with each other. The mean length of l^*_{vortex} is 0.09 and that of $l^*_{Nu_{D_h}}$ is 0.14. The mean value of the spanwise distance between the vortex centerline and the Nu_{D_h} peak line is 0.05. They are sometimes tilting each other but statistically aligned in parallel. These results strongly show that high Nu_{D_h} spindle-shaped spots on the wavy wall are generated by the action of streamwise vortices.

Fig. 8(a) and (b), respectively, shows the pdfs of the space mean vortex stretching term $\langle \tilde{\omega}_s(\partial \tilde{u}_s/\partial s)\rangle_c$ and of

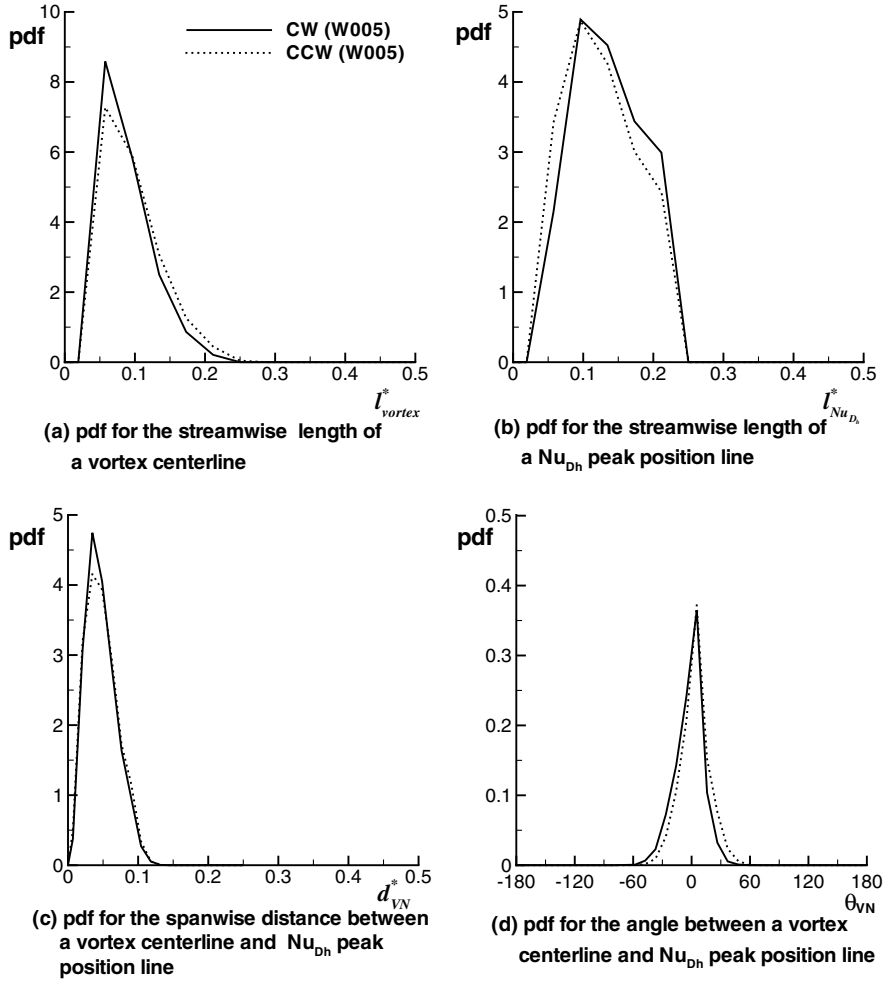

Fig. 7. Conditionally sampled probability density functions related to the vortex centerline and Nu_D peak position line for the W005 case.

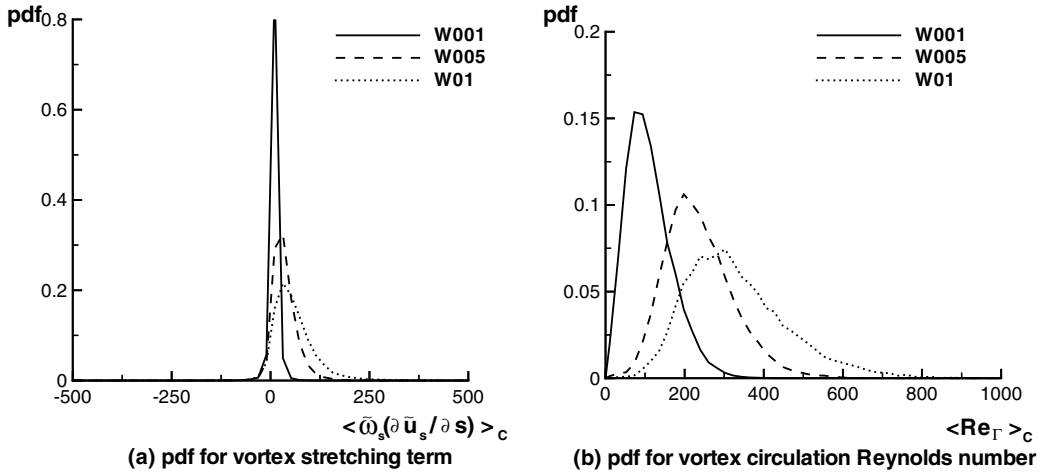

Fig. 8. Conditionally sampled probability density functions for $\langle \tilde{\omega}_s(\partial \tilde{u}_s/\partial s)\rangle_c$ and $\langle Re_\Gamma\rangle_c$ with varying wall wave amplitude.

the space mean vortex circulation Reynolds number $\langle Re_\Gamma\rangle_c$ for the vortices of *CW* case. As is seen in Fig. 8(a), probability of stretching rate is higher than the counterpart of shrinking one. In addition to that, with an increase of the slope of the wall, peak values of both pdfs become lower but they become broader. So, these figures clearly show that the streamwise vortices are intensified with an increase of wall wave amplitude due to the stronger stretching of the vortices resulting in much intense rotational flow fields around the vortices. This stronger vortex stretching comes from the larger flow acceleration rate along the steeper up-slope of the wall.

Fig. 9 shows the pdf of $\langle Nu_{D_h}\rangle_c$, the spatial mean of the peak value of Nu_{D_h} averaged along the Nu_{D_h} peak position line, together with $\overline{Nu}$, the space and time mean Nusselt number for the whole bottom wavy surface, and Nu_{trough}, the space and time mean Nusselt number only for the trough region of the bottom wavy surface for the three cases of different wall waviness. Nu_{trough} does not change so much with the change of wall waviness, but $\overline{Nu}$ increases noticeably with an increase of wall waviness. In a more noticeable way, the central value and bandwidth of $\langle Nu_{D_h}\rangle_c$ pdf increase with an increase of wall waviness.

In Fig. 10 the mean values of $\langle \tilde{\omega}_s(\partial \tilde{u}_s/\partial s)\rangle_c$, $\langle Re_\Gamma\rangle_c$ and $\langle Nu_{D_h}\rangle_c$ are replotted against the wall wave amplitude. All of the three quantities are confirmed to increase with an increase of wall waviness. All the results shown in Figs. 6–10 clearly show that the heat transfer enhancement to be achieved by the wall undulation is due to the streamwise vortices more densely generated in the up-slope part of the wavy wall with larger circulation at larger wall waviness.

Now, more detailed discussion will be given to how the wall heat transfer is enhanced by the streamwise vortices. Figs. 11–14 show the conditionally averaged velocity and temperature fields around the detected streamwise vortices. In these figures, $z^* = 0$ is the spanwise position of the center of the longitudinal vortices and Fig. 12 is for the counter-clockwise vortices and other three figures are for the clockwise ones. Fig.

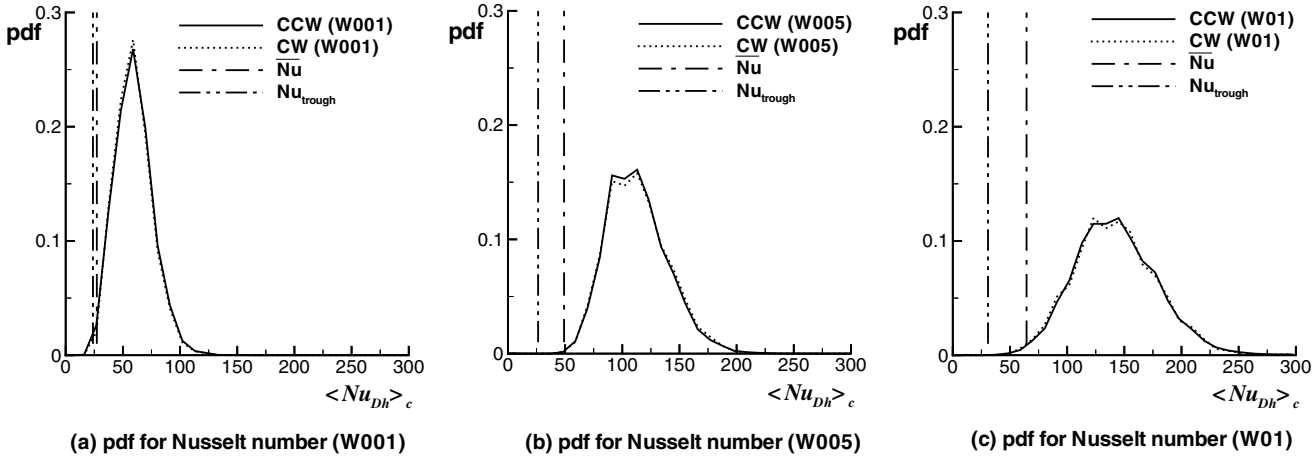

Fig. 9. Conditionally sampled probability density functions for $\langle Nu_{D_h}\rangle_c$ with varying wall wave amplitude.

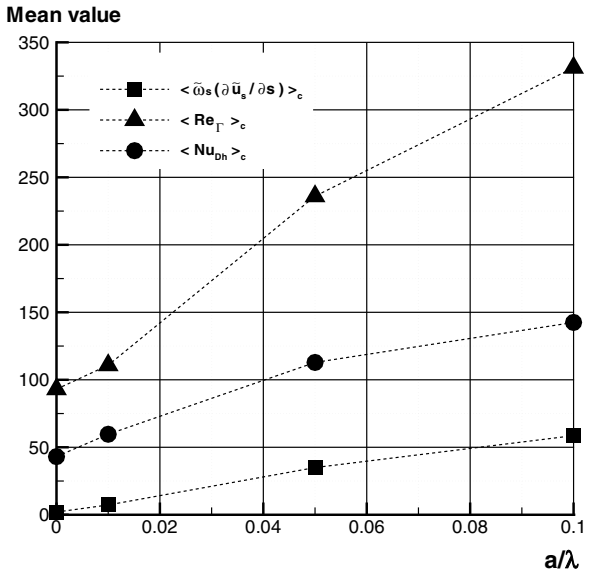

Fig. 10. Mean values of $\langle \tilde{\omega}_s(\partial \tilde{u}_s/\partial s)\rangle_c$, $\langle Re_\Gamma\rangle_c$ and $\langle Nu_{D_h}\rangle_c$.

11(a) and (b) shows the conditionally averaged contours respectively of $\langle Q_{V4}\rangle_{cs}$ and $\langle Q_{V6}\rangle_{cs}$ around the detected vortices in (y,z) cross-section obtained for the W005 case. In addition to these two figures, conditionally averaged contours of $\langle Q_{T4}\rangle_{cs}$ and $\langle Q_{T6}\rangle_{cs}$ in (y,z) cross-section are presented, respectively, in Fig. 11(c) and (d). At the bottom of Fig. 11(a) and (c), conditionally averaged skin friction coefficient and Nu_{D_h} are also plotted. Figs. 13 and 14 compare the values of $\langle Q_{T4}\rangle_{cs}$ and $\langle \partial\tilde{\theta}/\partial y\rangle_{cs}$, the conditionally averaged transverse fluid temperature gradient, for the three cases of different wall wave amplitude.

In Fig. 11(a), contour of the conditionally averaged value of Λ_2 is shown for the detected clockwise vortices. Counter-clockwise vortex sits on the left side of the clockwise one, but its existence cannot so sharply be observed. This is because the distance between the two vortices is different from one sample to another. Center of the clockwise one is located at $z^* = 0$ the same spanwise position but the counterpart of the counter-clockwise one differs from one sample to another. So, it should be noted that the velocity and temperature patterns around the counter-clockwise vortices are somehow smeared in this data processing procedure and similar smearing can be seen for the counter-clockwise vortices in Fig. 12. Down-wash flow appears both sides of the pair vortices and hot ejection-like event appears in between the two vortices. At the right edge of the clockwise vortex, down-wash flow is observed to exist, i.e., $v < 0$ and it conveys cooler fluid, i.e., $\theta < 0$, toward the wall. Therefore, $\langle Q_{T4}\rangle_{cs}$ for cold-sweep like event takes large value there as shown in Fig. 11(c). Both of the right side and left side down-wash flows are deflected inward so as to meet each other and wash the heat transfer surface beneath the vortices. So, around the down-wash flow and inward flow regions, thinner thermal conductive layer results in and the local Nusselt number becomes large there. On the other hand, leftward and rightward washing-wall flows are heated, merge with each other and form the up-wash flow. Although hot fluid is somehow taken away by the

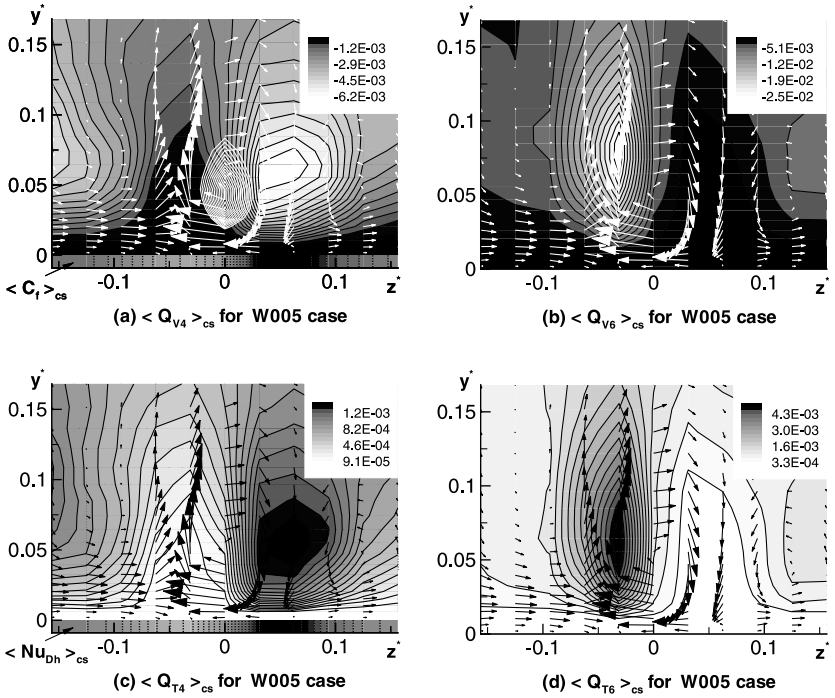

Fig. 11. Conditionally averaged (y,z) cross-sections at $x/\lambda = 0.94$ for the case W005 (CW).

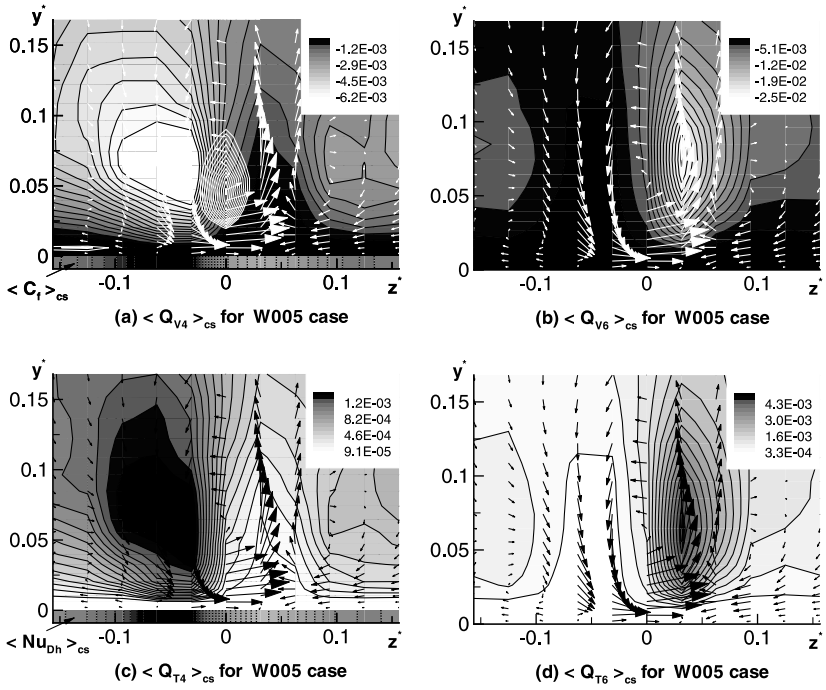

Fig. 12. Conditionally averaged (y, z) cross-sections at $x/\lambda = 0.94$ for the case W005 (CCW).

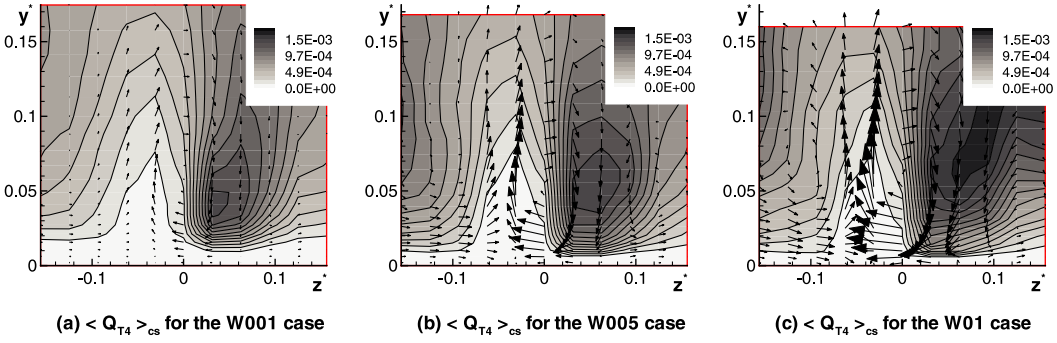

Fig. 13. Contours of conditionally averaged Q_{T4} at $x/\lambda = 0.94$ with varying wall wave amplitude.

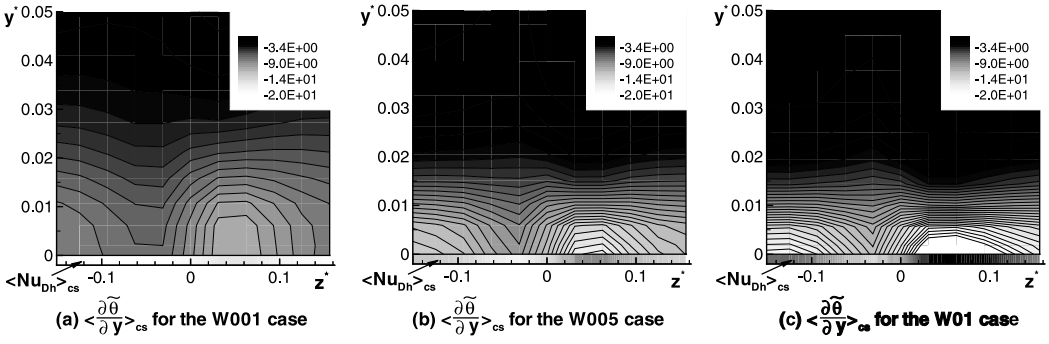

Fig. 14. Contours of conditionally averaged transverse temperature gradient at $x/\lambda = 0.94$ with varying wall wave amplitude.

up-wash flow as is confirmed in Fig. 11(d) by the high value of $\langle Q_{T6} \rangle_{cs}$, thermal conductive layer is much thicker just below the up-wash flow region. Therefore, the local Nusselt number remains low there. However, this is overcome by the increase of Nusselt number occurring beneath the vortices. This results in the enhancement of spatially averaged wall heat transfer as the effect of wall undulation. In the up-slope part of the bottom

wavy wall, streamwise vortices are densely generated and their intensity becomes larger with an increase of the wall wave amplitude (Choi et al., 2004). As a result, with an increase of wall undulation, $\langle Q_{T4}\rangle_{cs}$ is intensified and temperature gradient becomes steeper. This is confirmed in Figs. 13 and 14 and is consistent with the above discussed points that both of $\langle \tilde{\omega}_s(\partial \tilde{u}_s/\partial s)\rangle_c$ and $\langle Re_\Gamma\rangle_c$ become larger with an increase of wall undulation. Therefore, with increasing wall wave amplitude, the enhancement of the wall heat transfer is intensified as has been observed in Fig. 5.

For readers' information, relationship between the statistical characteristics of the turbulent flows in a channel with one wavy wall and the heat transfer enhancement is not discussed here but is discussed in the reference (Choi, 2004).

5. Conclusions

Large eddy simulation (LES) has been applied to the thermal fields of a turbulent flow in a channel having one wavy wall with various wall wave amplitude. To study the turbulent heat transfer characteristics of the flow, statistical and conditionally sampled thermal fields were scrutinized. Through the present study, the following conclusions are derived:

1. Both of C_f and Nu have the maximum value in the up-slope part of the wavy wall. Wall undulation is found to effectively enhance the wall heat transfer. With the increase of the wave amplitude from $a/\lambda = 0.01$ to $a/\lambda = 0.1$, C_f peak value becomes about three times larger and Nu peak value about four times larger.
2. Paying attention to instantaneous turbulent thermal fields, spindle-shaped high Nusselt number regions appear on the wavy wall in its up-slope part. Each region is located close and in parallel to an instantaneously generated streamwise vortex and this instantaneous near-wall streamwise vortex effectively elevates the instantaneous local wall heat transfer.
3. Systematic analysis of conditionally sampled turbulent thermal fields around the instantaneous near-wall streamwise vortices clearly shows that the primary source of vortex enhancement in the up-slope region is the vortex stretching accompanying the near-wall flow acceleration, and thus with increasing the wall wave amplitude the vortices are more effectively intensified. As a result, these phenomena greatly affect the wall heat transfer. The time and space averaged wall Nusselt number, $\overline{Nu}$, is mainly influenced by the thermal fields to be built-up around the near-wall streamwise vortices appearing densely in the up-slope part of the bottom wavy wall.
4. Conditionally sampled thermal fields around the identified near-wall streamwise vortices indicate that peak position of instantaneous wall Nusselt number is located below the place where the strong Q_{T4} event occurs. Furthermore, with increasing the wall wave amplitude, Q_{T4} events are observed to be intensified resulting in the augmentation of instantaneous local wall heat transfer around the streamwise vortices. This is the mechanism of wall heat transfer augmentation by the near-wall streamwise vortices in the wavy wall channel flows.

References

Choi, H.S., 2004. A numerical study on the turbulent flow and heat transfer in a channel with a wavy undulated bottom wall. Ph.D. Thesis, Kyoto University, Kyoto, Japan.

Choi, H.S., Park, T.S., Suzuki, K., 2004. Turbulence characteristics of the flows in a wavy channel. Int. J. Transport Phenom. 6 (3), 197–212.

De Angelis, V., Lombardi, P., Banerjee, S., 1997. Direct numerical simulation of turbulent flow over a wavy wall. Phys. Fluids 9, 2429–2442.

Eibeck, P.A., Eaton, J.K., 1987. Heat transfer effects of a longitudinal vortex embedded in a turbulent boundary layer. ASME J. Heat Transfer 109, 16–24.

Germano, M., Piomelli, U., Moin, P., Cabot, W.H., 1991. A dynamic subgrid-scale eddy viscosity model. Phys. Fluids 3, 1760–1765.

Henn, D.S., Sykes, R.I., 1999. Large-eddy simulation of flow over wavy surface. J. Fluid Mech. 383, 75–112.

Inaoka, K., Suzuki, K., 1995. Structure of the turbulent boundary layer and heat transfer downstream of a vortex generator attached to a LEBU plate. In: Durst, F., et al. (Eds.), Turbulent Shear Flows, vol. 9. Springer-Verlag, pp. 365–382.

Jeong, J., Hussain, F., 1995. On the identification of a vortex. J. Fluid Mech. 285, 69–94.

Jeong, J., Hussain, F., Schoppa, W., Kim, J., 1997. Coherent structures near the wall in a turbulent channel flow. J. Fluid Mech. 332, 184–214.

Kasagi, N., Ohtsubo, Y., 1995. Direct numerical simulation of low Prandtl number thermal field in a turbulent channel flow. Turbulent Shear Flows 8, 97–119.

Kasagi, N., Tomita, Y., Kuroda, A., 1992. Direct numerical simulation of passive scalar field in a turbulent channel flow. ASME J. Heat Transfer 114, 598–606.

Kida, S., Yanase, S., 2000. Ranryurikigaku (turbulence Mechanics), second ed. Asakura Shoten (in Japanese).

Lele, S.K., 1992. Compact finite difference schemes with spectral-like resolution. J. Comput. Phys. 103, 16–42.

Lilly, D.K., 1992. A proposed modification of the Germano subgrid-scale closure model. Phys. Fluids 4, 633–635.

Matsubara, K., Takeshi, M., Suto, H., Kobayashi, M., 2002. DNS study of turbulent flow and heat transfer over wavy surfaces. In: Proc. of the Twelfth International Heat Transfer Conference, pp. 195–200.

Mills, A.F., 1992. Heat Transfer, international student ed. Richard D. IRWIN, Homewood, IL.

Park, T.S., 1999. Multigrid method and low-Reynolds-number k–ε model for turbulent recirculating flows. Numerical Heat Transfer Part B: Fundamentals 36, 433–456.

Park, T.S., Choi, H.S., Suzuki, K., 2004. Nonlinear k–ε–f_μ model and its application to the flow and heat transfer in a channel having one undulation wall. Int. J. Heat Mass Transfer 47, 2403–2415.

Smagorinsky, J., 1963. General circulation experiments with the primitive equations: I. The basic equations. Mon. Whether Rev. 91, 99–164.

Suzuki, K., 1996. Flow modification and heat transfer enhancement with vortices. In: Proc. of Ninth International Symposium on Transport Phenomena, vol. 1, pp. 72–83.

Suzuki, K., Nakabe, K., 2002. Application of flow and temperature visualization to the study of longitudinal vortices and accompanying heat transfer enhancement. Keynote Paper. In: Tenth International Flow Visualization, Kyoto, August, pp. 26–29.

Suzuki, H., Suzuki, K., Sato, T., 1988. Dissimilarity between heat and momentum transfer in a turbulent boundary layer distributed by a cylinder. Int. J. Heat Mass Transfer 31, 259–265.

Suzuki, K., Inaoka, K., Kobayashi, M., Maekawa, H., Matsubara, K., 1998. Flow control and heat transfer enhancement with vortices. In: Notes on numerical fluid mechanics, vol. 63. Vortices and Heat Transfer, Vieweg-Verlag, pp. 356–378.

Vold, E.L., 1999. Computational simulations of vorticity enhanced diffusion. Phys. Fluids 11, 3353–3368.

Westphal, R.V., Eaton, J.K., Pauley, W.R., 1987. Interaction between a vortex and a turbulent boundary layer in a streamwise pressure gradient. Turb. Shear Flows 5, 266–277.

Wroblewski, D.E., Eibeck, P.A., 1991. Measurements of turbulent heat transfer in a boundary layer with an embedded streamwise vortex. Int. J. Heat Mass Transfer 34, 1617–1631.

You, J., Choi, H., Yoo, J.Y., 2000. A modified fractional step method of keeping a constant mass flow rate in fully developed channel and pipe flows. KSME Int. J. 14, 547–552.

Zhu, J., 1992. Higher-order bounded discretization schemes for finite volume computations of incompressible flows. Comput. Meth. Appl. Mech. Eng. 98, 345–360.